Modified Double Exchange Model with Novel Spin and Orbital Coupling: Phase Diagram of The Manganites

L. Sheng and C.S. Ting

Physics Department and Texas Center for Superconductivity, University of Houston, Houston, TX 77204

Abstract

From a general model of the Mn oxides $R_{1-x}A_x\mathrm{MnO_3}$, we derive an effective Hamiltonian in the low-energy subspace using the projection operator method, in which a novel coupling between the spin and orbital degrees of freedom is included. A phase diagram for temperature T versus doping concentration x is computed by means of Monte Carlo simulation. Our result is consistent with experimental observations in the Mn oxides with relatively wide conduction band, such as $\mathrm{Pr_{1-x}Sr_xMnO_3}$ and $\mathrm{La_{1-x}Sr_xMnO_3}$. According to the obtained orbital ordering, we also predict that the motion of charge carriers transforms from three-dimensional to two-dimensional as x is increased beyond a critical value.

PACS No: 75.30. Kz, 75.30.Et, 75.50.-y, 75.25.+z

The peculiar magnetic and transport properties including the colossal magnetoresistance (CMR) of the manganites $R_{1-x}A_x\mathrm{MnO_3}$ (where R =La, Nd or Pr and A =Ca, Sr, Ba or Pb) have become the main focus of many recent research activities. In undoped $R\mathrm{MnO_3}$, each Mn atom has four outshell $3d$ electrons, three localized t_{2g} electrons forming an $S = 3/2$ core spin, and one itinerant electron filling into two degenerate e_g orbitals, namely, $|+\rangle = d_{3z^2-r^2}$ and $|-\rangle = d_{x^2-y^2}$. $R\mathrm{MnO_3}$ is usually an A-type antiferromagnetic (A-AF) insulator [1,2], where the local spins are aligned ferromagnetically in layers parallel to the ab plane and antiferromagnetically along the c axis. Hole doping by partial substitution of R^{3+} atoms by A^{2+} atoms soon destroys the A-AF order, and strong ferromagnetism occurs for $0.1 \lesssim x \lesssim 0.4$ [3–6].

Near $x = 0.5$, the manganites exhibit different magnetic structures, as controlled by the conduction band width W. some manganites with relatively large W, such as $\mathrm{Pr_{0.5}Sr_{0.5}MnO_3}$ [5,7,8], are in an A-AF state below a critical temperature T_N and changes to a ferromagnetic (FM) state above T_N through a discontinuous phase transition. Some manganites with small W, e.g., $\mathrm{Pr_{0.5}Ca_{0.5}MnO_3}$ [9] and $\mathrm{La_{0.5}Ca_{0.5}MnO_3}$ [10], exhibit a more complicated CE-type antiferromagnetic (CE-AF) order with charge ordering at low temperatures, where the spins arrange ferromagnetically in zig-zag chains and antiferromagnetically between neighboring chains. In some other manganites with intermediate W, such as $\mathrm{Nd_{1-x}Sr_xMnO_3}$ [8,11], CE-AF and A-AF orders may coexist in the systems, and their volume fractions change rapidly with small change in x.

For further doping, the A-AF state appears to be the fundamental ground state spin configuration in many manganites. It has been observed in $\mathrm{La_{1-x}Sr_xMnO_3}$ with $0.52 < x < 0.58$ [12], $\mathrm{Nd_{1-x}Sr_xMnO_3}$ with $0.53 < x < 0.62$ [12] and $\mathrm{Pr_{1-x}Sr_xMnO_3}$ with $0.48 < x < 0.6$ [5]. Near the ending doping concentration $x = 1.0$, the manganites develop an isotropic G-type antiferromagnetic (G-AF) ground state [1]. In the region between $x \simeq 0.6$ and the ending concentration, most manganites are non-ferromagnetic insulators [4,12], but their microscopic spin structures have so far been seldom studied in experiments.

The conventional double exchange (DE) model [13–15] for the Mn oxides usually predicts strong ferromagnetism symmetrically about $x = 0.5$, which does not account for the antiferromagnetic phase at $x \gtrsim 0.5$ observed experimentally. While Jahn-Teller (J-T) effect [16,17], orbital degrees of freedom [18], and Coulomb interactions [5,18] have been proposed as necessary extensions of the DE model, theoretical phase diagram in the $T \sim x$ plane commensurating with experimental observations has yet to be obtained.

In this work, starting from a general model for the manganites we derive a modified DE Hamiltonian, which by comparison with the conventional DE model contains an orbital dependence in the hopping integral and a novel effective coupling between the spin and orbital degrees of freedom originating from the strong correlations. The magnetic and orbital phase diagram of this Hamiltonian is calculated using Monte Carlo simulation and simulated annealing technique [19]. Our results obtained are in good agreement with the experimental measurements in the manganites with relatively wide conduction band in the entire $T \sim x$ plane.

With the two-fold degeneracy of the e_g orbitals included, the total Hamiltonian for the Mn oxides can be written as

$$H = -\sum_{ij\alpha\beta} t_{ij}^{\alpha\beta} a_{i\alpha s}^{\dagger} a_{j\beta s} - K \sum_{i\alpha ss'} \boldsymbol{\sigma}_{ss'} \cdot \mathbf{s}_i a_{i\alpha s}^{\dagger} a_{i\alpha s'} + U \sum_{i\alpha} n_{i\alpha\uparrow} n_{i\alpha\downarrow}$$

$$+ U' \sum_{iss'} n_{i+s} n_{i-s'} + \frac{J_{\rm S}}{2} \sum_{ij} \mathbf{s}_i \cdot \mathbf{s}_j - g \sum_{i\alpha\beta s} \boldsymbol{\tau}_{\alpha\beta} \cdot \mathbf{Q}_i a^\dagger_{i\alpha s} a_{i\beta s} + \frac{k}{2} \sum_i Q_i^2 \ . \tag{1}$$

Here, $a_{i\alpha s}$ annihilates an electron at site i in e_g orbital $\alpha(=+,$ or $-)$ with spin $s(=\uparrow,$ or $\downarrow)$. K is the Hund's rule coupling between e_g electrons and localized spins, where $\boldsymbol{\sigma}$ are the Pauli matrices in the e_g spin space and $\mathbf{s}_i = \mathbf{S}_i/S$ a unit vector in the direction of the classical localized spin $\mathbf{S}_i$. U and U' represent the intraorbital and interorbital Coulomb repulsions, respectively. $J_{\rm S}$ stands for the superexchange coupling of the localized t_{2g} spins. g is the J-T coupling between the e_g electrons and local J-T lattice distortions $\mathbf{Q}_i$, where $\boldsymbol{\tau}$ are the Pauli matrices in the orbital space and $\mathbf{Q}_i = (Q_{ix}, Q_{iz})$ describes the two e_g modes of the J-T distortions. The orbital degrees of freedom are also called the isospin of the e_g electrons, for they are similar to the spin degrees of freedom. The orbital-dependent hopping integrals [18] $t_{ij}^{\alpha\beta}$ are elements of the 2×2 matrix $\hat{t}_{ij} = t(1 + \boldsymbol{\tau} \cdot \mathbf{n}_{ij})$. Here, $\mathbf{n}_{ij} = \mathbf{n}_\delta$ with $\delta = x, y,$ and z for hopping along the x, y and z direction, where $\mathbf{n}_x = (-\sqrt{3}/2, 0, -1/2)$, $\mathbf{n}_y = (\sqrt{3}/2, 0, -1/2)$ and $\mathbf{n}_z = (0, 0, 1)$ are three unit vectors distributed symmetrically in the $x - z$ plane. Introducing the three unit vectors is a key step in our theory, which will allow us to express the effective Hamiltonian in a compact and transparent form.

In the case of large U, U', K and J-T coupling g, we can derive an effective Hamiltonian in the low-energy subspace by following a similar procedure to the derivation of the $t - J$ model from the Hubbard model [20]. The total Fock space is divided into two subspaces: the low-energy subspace where each Mn site is occupied by at most one e_g electron and the spin and isospin of the e_g electron are parallel to local $\mathbf{s}_i$ and $\mathbf{Q}_i$, respectively, and the reminder subspace, namely, the high-energy subspace. Using the projection operator method and treating the kinetic energy term as a perturbation [20,21], we obtain an effective Hamiltonian in the low-energy subspace

$$\begin{aligned} H_{eff} = & - \sum_{ij} \widetilde{t}_{ij} d_i^\dagger d_j + \frac{J_{\rm S}}{2} \sum_{ij} (1 + \gamma n_i n_j) \mathbf{s}_i \cdot \mathbf{s}_j \\ & - \frac{J'}{2} \sum_{ij} n_i n_j (1 + \lambda \mathbf{s}_i \cdot \mathbf{s}_j)[1 - (\boldsymbol{\tau}_i \cdot \mathbf{n}_{ij})(\boldsymbol{\tau}_j \cdot \mathbf{n}_{ij})] \ , \end{aligned} \tag{2}$$

where $n_i = d_i^\dagger d_i$, and d_i annihilates an e_g electron with spin and isospin parallel to $\mathbf{s}_i$ and $\mathbf{Q}_i$. Here, $\gamma = 2I_3/J_{\rm S}$, $J' = I_1 + I_2 - I_3$, and $\lambda = (I_1 - I_2 + I_3)/J'$, where $I_1 = t^2/(U' + 2n_e E_J)$, $I_2 = t^2/(U' + 2n_e E_J + 2K)$ and $I_3 = t^2/(U + 2K)$ with $E_J = g^2/k$ as the $J - T$ energy and $n_e = 1 - x$ as the average electron density. The isospin and lattice distortion are forced mutually parallel by the strong J-T coupling. $\boldsymbol{\tau}_i$ is a unit vector describing the orientation of the isospin or which orbital state on Mn site i is occupied by an e_g electron. If $\boldsymbol{\tau}_i$ makes an angle ϕ_i with the z axis, then the e_g electron at site i occupies the orbital state

$$|\phi_i\rangle = \cos(\phi_i/2) d_{3z^2-r^2} + \sin(\phi_i/2) d_{x^2-y^2} \ , \tag{3}$$

and it also represents the direction of the lattice distortion; i.e, $\boldsymbol{\tau}_i = \mathbf{Q}_i/Q_i$. The effective hopping integral in Eq. (2) can be written as

$$\widetilde{t}_{ij} = t\sqrt{(1 + \mathbf{s}_i \cdot \mathbf{s}_j)/2}\sqrt{(1 + \boldsymbol{\tau}_i \cdot \mathbf{n}_{ij})(1 + \boldsymbol{\tau}_j \cdot \mathbf{n}_{ij})} \ . \tag{4}$$

The first square root together with t is the well-known hopping integral in the conventional DE model [13], and the last term describes the dependence on the orbital alignments.

Equation (2) is a modified DE model. The main merit of this model is that it contains only weak couplings between classical fields $\mathbf{s}_i$ and $\boldsymbol{\tau}_i$. To show its relevance to the Mn oxides, we shall calculate the magnetic and orbital phase diagram. Focusing on the spin and isospin dynamics, we replace the charge operators in Eq. (2) by their averages $n_i \simeq n_e$ and $d_i^\dagger d_j \simeq \langle d_i^\dagger d_j \rangle$. We further approximate $\langle d_i^\dagger d_j \rangle \simeq \langle d_i^\dagger d_j \rangle_0$ with $\langle d_i^\dagger d_j \rangle_0$ as the average of $d_i^\dagger d_j$ in a tight binding model. The resulting spin and isospin Hamiltonian is classic and can be studied by using Monte Carlo simulations together with simulated annealing technique [19]. We start from a sufficiently high temperature $k_B T = 0.2t$ and work on a $14 \times 14 \times 14$ cubic lattice. The temperature is decreased by 8% each step. For each step, about 2×10^6 spin and isospin configurations are sampled, and thermal average is calculated after initial sampling of 5×10^5 configurations.

We consider first the undoped case, where $n_e = 1$ or $x = 0$ and the kinetic energy term in Eq. (2) vanishes. The ground state depends on only two dimensionless parameters λ and J'/J where $J = J_{\rm S}(1+\gamma)$. In the Monte Carlo simulation, as the temperature is decreased to a sufficiently low value, e.g., $k_B T = 10^{-2} J$, the spins and isospins will eventually develop their ground state configurations, which can be examined directly. Numerical calculation indicates totally four possible ground states: G-AF, C-AF, A-AF and FM, where in the C-AF state the local spins arrange ferromagnetically in parallel chains and antiferromagnetically between neighboring chains. In all the four magnetic states, the e_g electrons occupy two different orbital states on two sublattices, exhibiting alternating orbital order. For the FM and G-AF states, the e_g electrons occupy an arbitrary pair of orthogonal orbital states in the two sublattices. For the A-AF state, the occupied orbital states in the two sublattices are $(d_{3z^2-r^2} + d_{x^2-y^2})/\sqrt{2}$ and $(d_{3z^2-r^2} - d_{x^2-y^2})/\sqrt{2}$. For the C-AF state, the two occupied orbital states are $d_{3x^2-r^2}$ and $d_{y^2-z^2}$, if the ferromagnetic chains are assumed along the y direction. The obtained phase diagram in the λ versus J'/J plane is given in Fig. 1. The phase transition between different phases with changing the parameters is of first order.

In order to ensure an A-AF ground state for undoped $R\mathrm{MnO_3}$, the parameters have to be chosen in the shaded region of Fig. 1. We will hereafter choose $J_{\rm S} = 0.03t$, $U = 42t$, $U' = 7t$, $E_J = 3.5t$ and $K = 9t$ as reasonable values for the Mn oxides, which correspond to the point indicated by the triangle in Fig. 1 for the undoped case. The phase diagram in the normalized temperature $k_B T/t$ versus doping concentration x plane is obtained numerically by calculating simultaneously various long-range order parameters such as the magnetization M and short-range correlation functions of the localized spins such as $\langle \mathbf{s}_i \cdot \mathbf{s}_j \rangle$ in three directions, as well as those of the isospins, as functions of $k_B T/t$ and x. The resulting phase diagram is shown in Fig. 2.

In our phase diagram Fig. 2, there are an A-AF, a G-AF and a FM phase at low temperatures for $x \simeq 0$, $x \simeq 1.0$ and $0.1 \lesssim x \lesssim 0.4$, respectively, which are consistent with experiments in most manganites [1–6]. More importantly, we also observe an A-AF state for $0.6 \lesssim x \lesssim 0.9$ and a first-order FM to A-AF phase transition upon cooling around $x \simeq 0.5$ [as will also be seen in Fig. (4)]. This result agrees well with the experimental measurements in the manganites with relatively wide conduction band, e.g., $\mathrm{Pr_{1-x}Sr_xMnO_3}$ [5,7,8]. It is also possible, by slightly tunning the input parameters, to make our phase diagram more comparable to that of $\mathrm{La_{1-x}Sr_xMnO_3}$, where a FM state exists at $0.1 \lesssim x \lesssim 0.5$ [6] and an

A-AF state occurs for $x > 0.52$ [12].

The magnetization M normalized by the saturation magnetization $M_{\rm S}$ calculated using Monte Carlo technique is shown in Fig. 3 as a function of the normalized temperature for several values of doping concentration. For $x = 0.1$, 0.2 and 0.3, the magnetization approaches the saturation value M_s at low temperatures, exhibiting strong ferromagnetism in this doping range. The magnetization for $x = 0.4$ drops sharply from a large value to zero at a low critical temperature, corresponding to a first-order FM to A-AF phase transition.

Let us consider $x = 0.5$. In Fig. 4, the magnetization for different values of applied magnetic field is shown as a function of the normalized temperature. At zero magnetic field the magnetization first increases with decreasing temperature and then drops abruptly, after which the system enters an A-AF state. This magnetization curve resembles that measured in the Mn oxide $Pr_{0.5}Sr_{0.5}MnO_3$ [7]. With increasing the magnetic field, the magnetization increases obviously. For $2\mu_B S^* H/t = 0.024$, which corresponds to $H \simeq 20T$ if t is taken to be 0.2eV as a reasonable value for the Mn oxides, the magnetization reaches about 30% even at very low temperatures. The sensitivity of the magnetization to the magnetic field may explain the sharp resistivity drop induced by applied magnetic field observed in the low-temperature A-AF phase of $Pr_{0.5}Sr_{0.5}MnO_3$ [7].

Now we discuss the orbital structures in the phase diagram. As seen from the inset of Fig. 2, there are two different ground state orbital structures. In the region denoted by "antiparallel", the e_g electrons occupy two different orbital states $(d_{3z^2-r^2} + d_{x^2-y^2})/\sqrt{2}$ and $(d_{3z^2-r^2} - d_{x^2-y^2})/\sqrt{2}$ in two sublattices, forming alternating orbital order. In the region denoted by "parallel", the e_g electrons occupy the same orbital $d_{x^2-y^2}$ on each site, showing uniform orbital order. The spatial distribution of the charge density or the square of the orbital wave function in the two types of orbital orders is illustrated in Fig. 5. It is interesting to notice that the antiparallel orbital order can be reguarded approximately as between $d_{3y^2-r^2}$ and $d_{3x^2-r^2}$, because the overlaps between these two sets of wave functions are larger than 97%. This result is in good agreement with the orbital order measured in $LaMnO_3$ using resonant X-ray scattering [22]. By substituting the orbital wave functions into the Hamiltonian Eq. (2), it is straightforward to obtain an anisotropic DE Hamiltonian for the charge carriers

$$H_{eff} = -t \sum_{ij} g_{ij} \sqrt{(1 + \mathbf{s}_i \cdot \mathbf{s}_j)/2}\; d_i^\dagger d_j \;, \tag{5}$$

where g_{ij} assumes different values $g_\parallel$ and $g_\perp$ in the ab plane and along the c axis. For the antiparallel orbital order, $g_\parallel = 1/2$ and $g_\perp = 1$, the motion of the charge carriers is three-dimensional. For the parallel orbital order, $g_\parallel = 3/2$ and $g_\perp = 0$, the charge motion is of two-dimensional nature. According to Eq. (5), the charge band width is $W = 8t$ for the antiparallel orbital order, and $W = 12t$ for the parallel orbital order, indicating that the kinetic energy term favors parallel orbital order. The kinetic energy will compete with the effective spin-orbital coupling which is favorable for antiparallel orbital order. The spin-orbital coupling is proportional to $n_i n_j \sim (1-x)^2$ according to Eq. (2). For small x, the spin-orbital coupling dominates and leads to antiparallel orbital order, in which the charges can move in three dimensions. This explains the appearance of the FM state for $0.1 \lesssim x \lesssim 0.4$ in the phase diagram Fig. 2. For large x, the spin-orbital coupling reduces, the kinetic energy dominates and leads to parallel orbital order. In this case, the charge

hopping is confined in two-dimensional planes, and so is the DE ferromagnetic coupling. The net interplane spin interaction then comes only from the antiferromagnetic superexchange coupling. As a result the A-AF order occurs.

In summary, we have established a modified DE model to describe the spin and orbital properties in the Mn oxides. The obtained phase diagram is consistent with experimental observations in the Mn oxides with relatively large conduction band width, such as $Pr_{1-x}Sr_xMnO_3$ and $La_{1-x}Sr_xMnO_3$, where the effect of long-range Coulomb interactions may be unimportant and the charge ordering is absent or rather weak. We expect that the present model can be further extended to describe the CE-AF state with charge ordering observed in systems with relatively narrow conduction band by including long-range Coulomb interactions.

This work was supported by the Texas Center for Superconductivity at the University of Houston through a grant from the state of Texas, by Texas ARP No: 3652707, and by the Robert A. Welch foundation.

REFERENCES

[1] E.O. Wollan and W.C. Koehler, Phys. Rev. **100**, 545 (1955).
[2] F. Moussa, *et al.*, Phys. Rev. B **54**, 15149 (1996).
[3] Y. Yamada, O. Hino, S. Nohdo, and R. Kanao, Phys. Rev. Lett. **77**, 904 (1996); A. Urushibara *et al.*, Phys. Rev. B **51**, 14103 (1995).
[4] P. Schiffer, A.P. Ramirez, W. Bao and S-W. Cheong, Phys. Rev. Lett. 3336 (1995).
[5] R. Maezono, S. Ishihara and N. Nagaosa, Phys. Rev. B **57**, R13993 (1998); Phys. Rev. B **58**, 11583 (1998).
[6] A. Urushibara *et al.*, Phys. Rev. B **51**, 14103 (1995).
[7] Y. Tomioka *et al.*, Phys. Rev. Lett. **74**, 5108 (1995).
[8] H. Kawano *et al.*, Phys. Rev. Lett. **78**, 4253 (1997).
[9] Z. Jirak *et al.*, J. Magn. Magn. Mater. **53**, 153 (1985); Y. Tomioka *et al.*, J. Phys. Soc. Jpn. **64**, 3626 (1995).
[10] S. Mori, C.H. Chen and S-W Cheong, Nature (London) **392**, 473, (1998); Phys. Rev. Lett. **81**, 3972 (1998).
[11] H. Kuwahara *et al.*, Science **270**, 961 (1995); M. Kubota *et al.*, cond-mat/9811192 (Nov. 1998).
[12] T. Akimoto *et al.*, Phys. Rev. B **57**, R5594 (1998).
[13] C. Zener, Phys. Rev. **82**, 403 (1951); P. W. Anderson and H. Hasegawa, *ibid* **100**, 675 (1955); P. -G. de Gennes, *ibid* **118**, 141 (1960).
[14] N. Furukawa, J. Phys. Soc. Jpn. **63**, 3214 (1994).
[15] E. Müller-Hartmann and E. Daggoto, Phys. Rev. B**54**, R6819 (1996); C.M. Varma, *ibid* **54**, 7328 (1996).
[16] A.J. Millis, P.B. Littlewood, and B.I. Shraiman, Phys. Rev. Lett. **74**, 5144 (1995); A.J. Millis, B. Shraiman and R. Mueller Phys. Rev. Lett. **77**, 175 (1996).
[17] H. Roder, J. Zang, and A.R. Bishop, Phys. Rev. Lett. **76**, 1356 (1996).
[18] S. Ishihara, J. Inoue and S. Maekawa, Phys. Rev. B **55**, 8280 (1997); S. Ishihara, M. Yamanaka and N. Nagaosa, *ibid* **56**, 686 (1997).
[19] *Monte Carlo Methods in Statistical Physics*, edited by K. Binder (Springer-Verlag, Berlin, 1979).
[20] *Interacting Electrons and Quantum Magnetism*, Edited by A. Auerbach, (Springer-Verlag, New York, 1994).
[21] L. Sheng, D.N. Sheng and C.S. Ting, unpublished.
[22] Y. Murakami *et al.*, Phys. Rev. Lett. **81**, 582 (1998).

FIGURES

FIG. 1. Phase diagram at $x = 0$ in the λ vs J'/J plane where $J = J_{\rm S}(1 + \gamma)$.

FIG. 2. Phase diagram in the k_BT/t vs x plane with PM as the paramagnetic phase. The dashed line indicates the boundaries of the orbital phases. Inset is the orbital phase diagram, where "antiparallel" stands for alternating orbital order between $(d_{3z^2-r^2} + d_{x^2-y^2})/\sqrt{2}$ and $(d_{3z^2-r^2} - d_{x^2-y^2})/\sqrt{2}$, and "parallel" indicates uniform $d_{x^2-y^2}$ orbital order.

FIG. 3. Calculated magnetization curves for several values of doping concentration x.

FIG. 4. Calculated magnetization curves for $x = 0.5$ at several values of magnetic field.

FIG. 5. Illustration of the spatial electron density distribution in (a) alternating orbital ordering state between $(d_{3z^2-r^2} + d_{x^2-y^2})/\sqrt{2}$ and $(d_{3z^2-r^2} - d_{x^2-y^2})/\sqrt{2}$, and (b) uniform $d_{x^2-y^2}$ orbital ordering state.

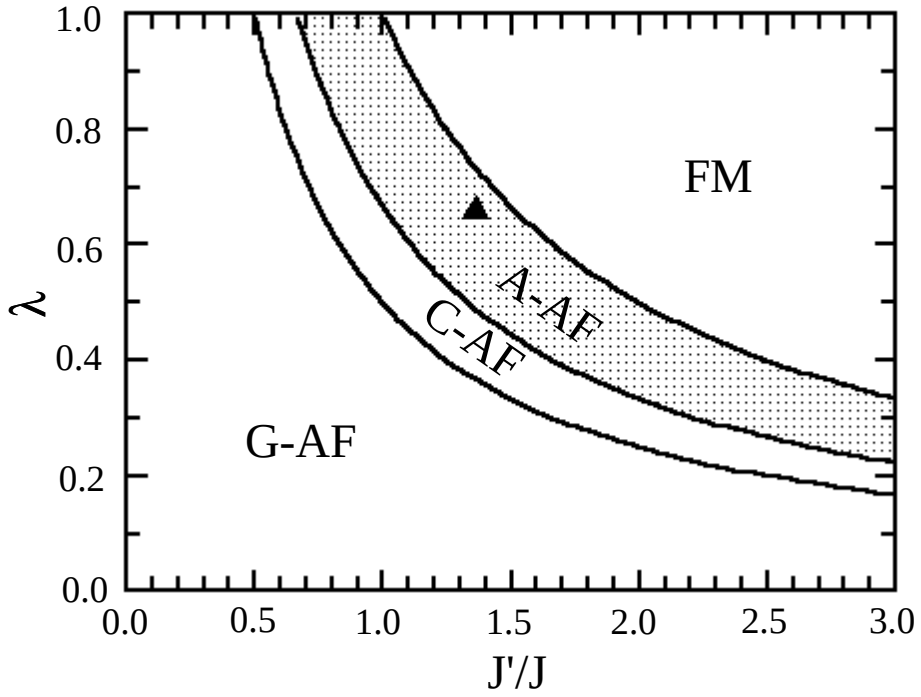

Fig. 1 (Sheng *et al*.)

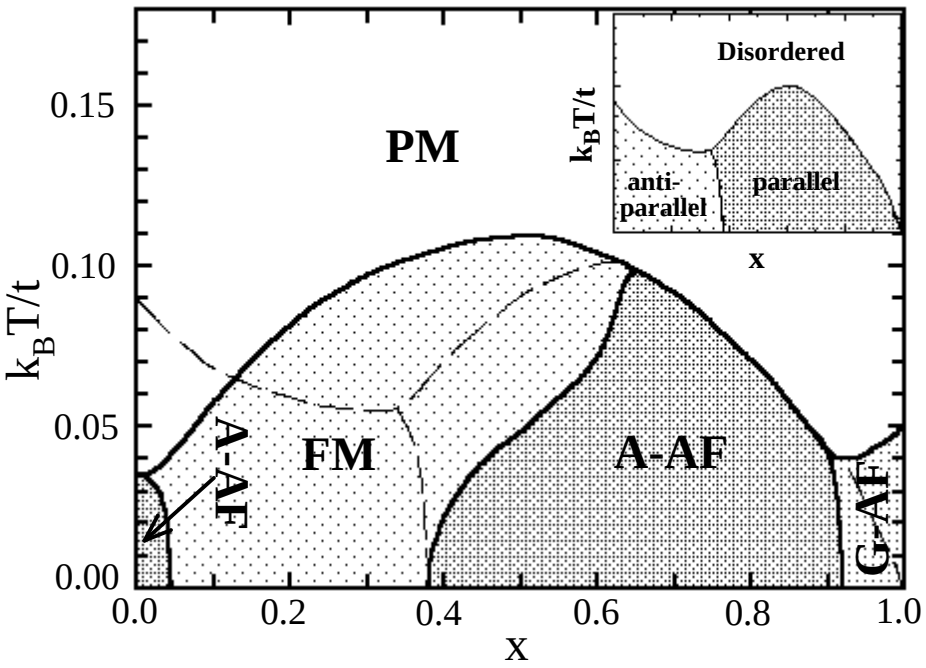

Fig. 2 (Sheng *et al*.)

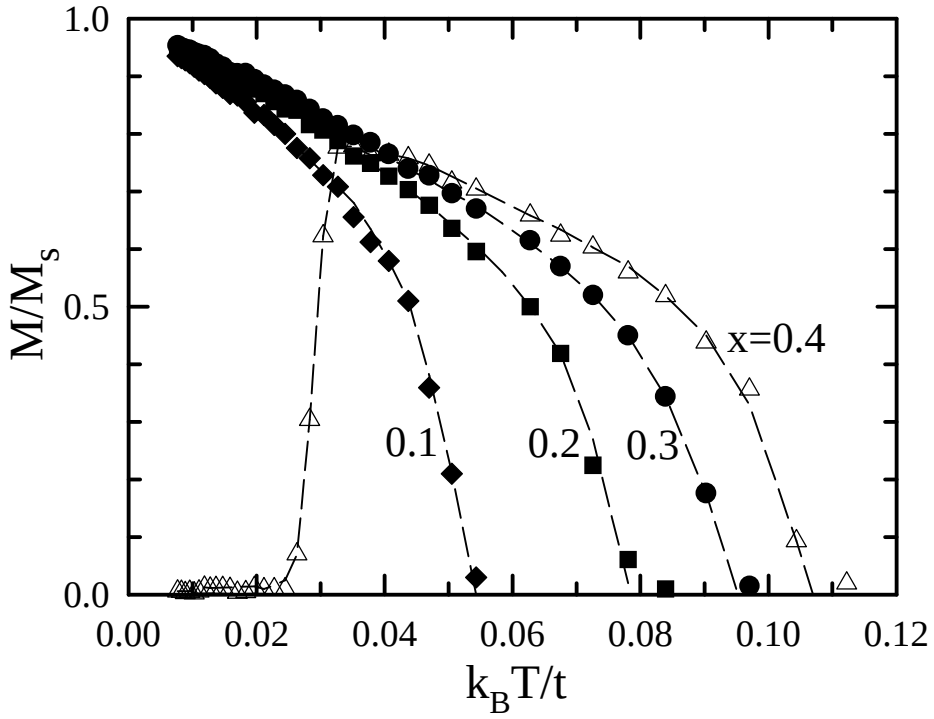

Fig. 3 (Sheng *et al*.)

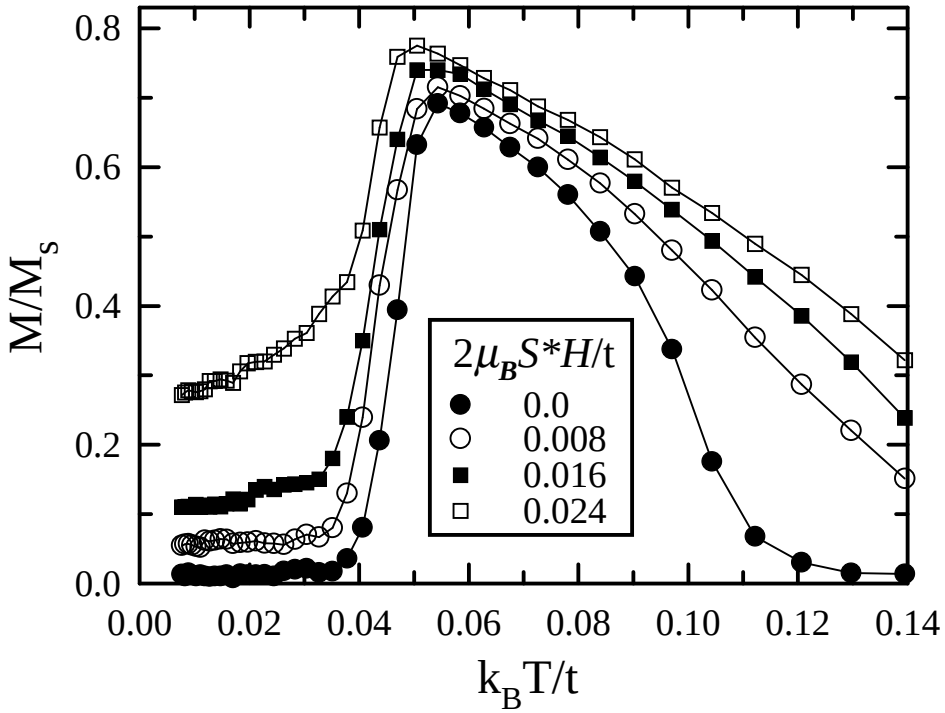

Fig. 4 (Sheng *et al*.)

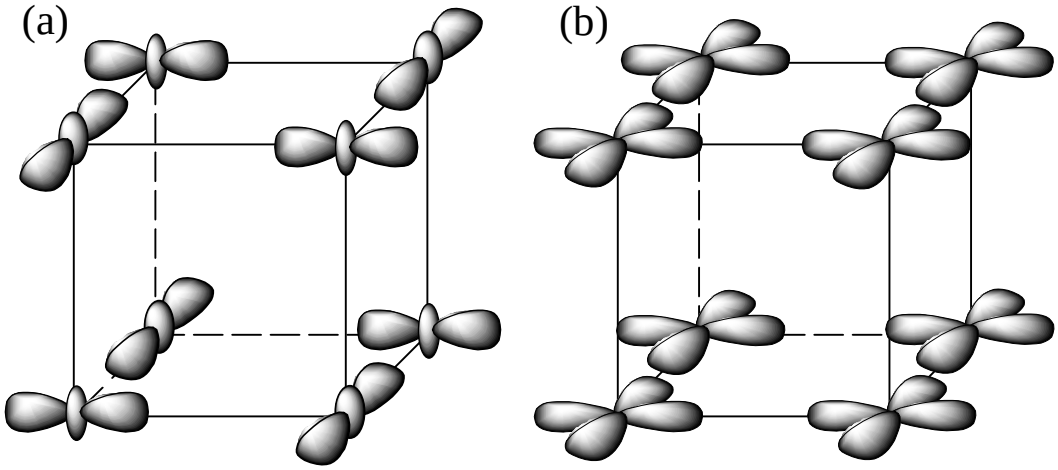

Fig. 5 (Sheng *et al*.)